






RESEARCH ARTICLE | JULY 05 2022

Double-layer acoustic metasurface for the suppression of the Mack second mode in hypersonic boundary-layer flow

Xudong Tian ; Tuo Liu  ; Tiantian Wang ; Jie Zhu  ; Chihyung Wen 



Physics of Fluids 34, 074105 (2022)

<https://doi.org/10.1063/5.0096772>



Articles You May Be Interested In

An asymptotic theory formulating the surface ablation impact on Mack modes in high-enthalpy hypersonic boundary layers

Physics of Fluids (September 2024)

Effect of porous coatings on the nonlinear evolution of Mack modes in hypersonic boundary layers

Physics of Fluids (May 2023)

Impact of continuously extending/retracting wall on Mack-mode evolution in hypersonic boundary layers

Physics of Fluids (November 2024)



Physics of Fluids

Special Topics Open
for Submissions

[Learn More](#)

Double-layer acoustic metasurface for the suppression of the Mack second mode in hypersonic boundary-layer flow

Cite as: Phys. Fluids **34**, 074105 (2022); doi: 10.1063/5.0096772

Submitted: 21 April 2022 · Accepted: 19 June 2022 ·

Published Online: 5 July 2022



View Online



Export Citation



CrossMark

Xudong Tian,¹ Tuo Liu,^{2,a)} Tiantian Wang,¹ Jie Zhu,^{3,a)} and Chihyung Wen⁴

AFFILIATIONS

¹Key Laboratory of Traffic Safety on Track, School of Traffic Transportation Engineering, Central South University, 410075 Hunan, China

²Key Laboratory of Noise and Vibration Research, Institute of Acoustics, Chinese Academy of Sciences, Beijing 100190, China

³Institute of Acoustics, School of Physics Science and Engineering, Tongji University, Shanghai 200092, China

⁴Department of Aeronautical and Aviation Engineering, The Hong Kong Polytechnic University, Hung Hom, Kowloon, Hong Kong SAR, China

^{a)}Authors to whom correspondence should be addressed: liutuo@mail.ioa.ac.cn and jiezhutongji.edu.cn

ABSTRACT

An acoustic metasurface consisting of two layers of perforated plates is proposed for suppression of the Mack second mode in hypersonic boundary-layer flow. The upper layer with very tiny holes is permeable to acoustic waves and hardly alters the background hypersonic boundary-layer flow, offering rather low resistive and inductive components of surface acoustic impedance. The bottom layer with large and sparse square holes is attached to a rigid wall surface and forms a periodic array of chambers, each covering multiple holes of the upper layer, which can adjust the impedance phase by working as a capacitive component. Based on a linear stability analysis of hypersonic boundary-layer instability, such an acoustic metasurface satisfying the required surface impedance is designed and numerically investigated. The results show that the metasurface can efficiently suppress the Mack second mode over a relatively wide bandwidth. This work provides an alternative strategy for the design of porous walls for hypersonic boundary-layer stabilization.

Published under an exclusive license by AIP Publishing. <https://doi.org/10.1063/5.0096772>

I. INTRODUCTION

The study of laminar–turbulent transition in hypersonic boundary layers is pivotal to the development of hypersonic flight vehicles owing to the pronounced differences in skin friction and heat transfer between these two flow regimes. In a low-disturbance flight environment, the linear growth of perturbations within a hypersonic boundary layer over a flat plate or an axisymmetric slender body at zero angle of attack is dominated by the Mack second mode.¹ Therefore, the boundary-layer transition may be delayed by reducing the growth rate of the second mode. Previous experimental results revealed that the frequency of the second mode is commonly above 100 kHz.^{2–6} Given the acoustic nature of this unstable mode, Fedorov *et al.*⁷ proposed that an ultrasonic absorptive coating (UAC) might be used to stabilize the second mode by absorbing the perturbation energy. Later, the stabilizing effect of porous coatings on hypersonic boundary layers was validated by experimental^{4,8–10} and theoretical¹¹ studies. Notably, the surfaces of the thermal protection systems (TPS) of hypersonic

vehicles are compatible with porous coatings. Therefore, porous coatings have been recognized as a promising approach to hypersonic boundary-layer control.¹²

For the design of porous coatings, Brès *et al.*¹³ proposed guidelines to estimate the depth of the pore holes required to achieve the minimum reflection coefficient for the most-unstable second mode, namely, $H/\lambda = (2n - 1)/4$, where H is the hole depth, λ is the wavelength of the incident wave, and $n = 1, 2, 3, \dots$. Brès *et al.*¹⁴ further found that a coating with relatively deep pores operates in an attenuative regime for second-mode instability, while a coating with relatively shallow pores operates in the cancellation or reinforcement regime, which depends on the frequency of the second-mode waves. By considering the mutual coupling of acoustic waves among neighboring cavities, Zhao *et al.*¹⁵ developed an improved model to describe the acoustic characteristics of porous coatings. In essence, a porous coating alters the boundary condition from a rigid wall to an impedance boundary and consequently changes the behavior of the Mack second

mode. In this regard, Zhao *et al.*¹⁶ revealed the role that surface acoustic impedance plays beyond energy absorption during second-mode suppression and suggested that an impedance magnitude as low as possible can lead to optimal performance. To realize near-zero surface impedance, they also introduced the concept of acoustic metasurfaces, a type of artificial structures with subwavelength thickness for unconventional acoustic wave manipulation,¹⁷ into the field of hypersonic boundary-layer control. Tian *et al.*¹⁸ further showed that the admittance phase, in addition to the reflection coefficient that was the focus of most previous work, is significant for stabilization of the Mack second mode by porous coatings.

In practice, it is difficult to implement near-zero impedance for high-frequency acoustic waves, especially for broadband disturbances. There is an intrinsic conflict between, on the one hand, the requirement of low impedance magnitude (larger cavities, generally) for second-mode control and, on the other hand, the requirement that surface structures should be as small as possible to guarantee negligible disturbances to hypersonic flow fields.^{4,19} It remains challenging to efficiently control the development of the second mode without interfering with the flow field itself. Notably, the minimum-reflection type of UAC is restricted by the excessive acoustic thermal-viscous losses reflected in the real part of the overall surface impedance, which becomes larger for narrower regions. Moreover, a large real part of the surface impedance imposes limits on the parameter range of the impedance phase, which may exclude the appropriate impedance value and is unfavorable for the design of commonly seen UACs composed of micro-holes or slits.¹⁸ To overcome the aforementioned conflict, we present here an acoustic metasurface that has negligible influence on the hypersonic boundary-layer flow, but can still be adjusted to achieve the surface impedance (or admittance) required by second-mode control. This functionality is enabled by our newly proposed double-layer design that offers additional flexibility in surface impedance engineering. Specifically, the upper perforated layer has thin and tiny openings only permeable to sound, providing acoustic resistance and inductance, while the bottom layer forms an array of relatively large cavities having an almost purely capacitive component to facilitate tuning of the impedance phase. Although similar ideas can be found in designs of sound-absorbing structures, their application to hypersonic boundary layer control has not previously been reported.

The remainder of the paper is organized as follows. In Sec. II, we describe the theoretical model and methods. In Sec. III, we analyze the effect of wall impedance on the stability of the hypersonic boundary layer and then apply the results to the metasurface design. In Sec. IV,

we examine the performance of the designed acoustic metasurface. Finally, we present the conclusions of this study in Sec. V.

II. MODEL AND METHODS

A. Metasurface and impedance model

The proposed acoustic metasurface consists of two layers: the upper layer that serves as the wall of the boundary-layer flow is a micro-perforated thin plate only permeable to ultrasonic waves, while the bottom layer is composed of relatively large square chambers to alter the reactance and thereby adjust the admittance phase, as shown in Fig. 1. Such a configuration allows for rather small structures that interact directly with the boundary-layer flow while providing sufficiently high admittance (low impedance) to control the second mode. In addition, compared with porous walls composed of regular micro-holes, this acoustic metasurface has greater flexibility in terms of design, since the inductive component and the capacitive component of the overall surface impedance are independently governed by the two layers, as will be discussed below.

In the low-frequency approximation (with the structure size much smaller than the wavelength), the specific impedance of the upper layer normalized by the characteristic impedance of air, ρc (ρ is the density and c is the speed of sound), is given by Refs. 20–23 as

$$Z_1 = Z_{1r} + iZ_{1i} \quad (1)$$

with

$$Z_{1r} = \frac{32\mu h}{\phi \rho c d^2} \sqrt{1 + \frac{K^2}{32} + \frac{2\alpha R_s}{\phi \rho c}}, \quad (2)$$

$$Z_{1i} = \frac{\omega(h + l_e)}{\phi c} \left(1 + \frac{1}{\sqrt{9 + 0.5K^2}} \right), \quad (3)$$

where $K = d\sqrt{(\omega\rho/\mu)}/2$, $l_e = 8d\Psi_{\text{Fok}}(\phi)/(3\pi)$ is the reactive end length correction, $\Psi_{\text{Fok}}(\phi)$ is the Fok function,²³ $\phi = n\pi d^2/(4S)$ is the porosity, d is the hole diameter, S is the cross-sectional area of a unit cell, n is the number of holes in a unit cell, h is the layer thickness, ω is the angular frequency, and μ is the viscosity coefficient. The second term on the right-hand of Eq. (2) represents the resistive end correction²² with $R_s = 0.5\sqrt{2\mu\rho\omega}$ and $\alpha = (14.1h/d + 117)/\sqrt{\omega/(2\pi)}$. In the bottom layer, the chamber has a much larger cross-sectional area than that of the perforations, and so its resistance can be neglected.²⁰ Thus, the cavity's impedance is purely imaginary and takes the form²¹

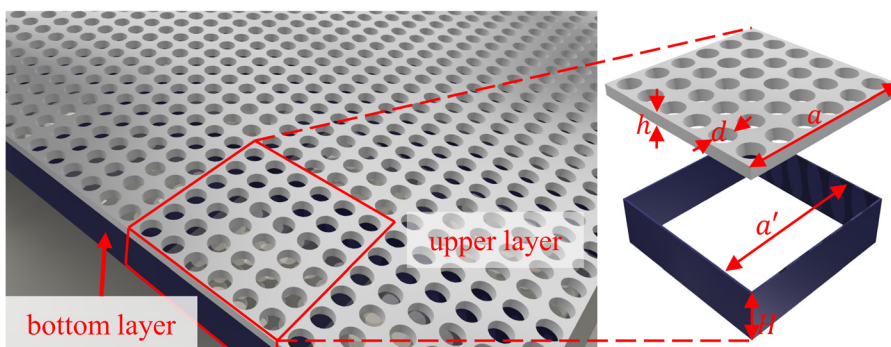


FIG. 1. Schematic of the double-layer acoustic metasurface. The metasurface consists of one upper micro-perforated plate (thickness h) with n evenly spaced holes (diameter d) in a unit cell (cross-sectional area $S = a \times a$) and one lower plate (thickness H) with relatively large and sparse square holes (cross-sectional area $S' = a' \times a'$). The inset shows one unit cell.

$$Z_2 = -i \frac{S}{S'} \cot\left(\frac{\omega H}{c}\right), \quad (4)$$

where H and S' are, respectively, the depth and cross-sectional area of the cavity. The total impedance of the whole system is the sum of these two individual impedances, namely,

$$Z = Z_1 + Z_2. \quad (5)$$

Note that Z_1 contains only resistive [$\text{Re}(Z_1) > 0$] and inductive [$\text{Im}(Z_1) > 0$] components, and Z_2 contains only capacitive [$\text{Im}(Z_2) < 0$] component in the low-frequency regime. The two layers form a periodic array of Helmholtz-like resonators embedded in the surface. In this study, we assume that the temperature of the metasurface is uniform and identical to the wall temperature of the boundary-layer flow, which is reasonable, since the flow in the microstructure is quasistatic and the metasurface will be made of thin metal with high thermal conductivity. Accordingly, the parameters ρ , c , and μ are approximated by the corresponding values at the wall, namely, ρ_w , c_w , and μ_w , in which μ_w is calculated using Sutherland's law.

To numerically validate the above impedance model of the actual metasurface structure, an acoustic finite-element simulation in the absence of a flow field is performed using the acoustics module of the commercial software COMSOL Multiphysics, in which the linearized acoustic wave equation is solved by the direct solver MUMPS (multifrontal massively parallel sparse direct solver). Specific to our simulation model, one unit cell is connected to a straight virtual impedance tube with cross section the same as the square lattice. The simulated reflection amplitude and phase (fundamental waveguide mode) for normal incidence are then used to extract the effective surface impedance.²⁴

B. Linear stability theory

Linear stability theory (LST) is predominantly utilized to calculate the eigenmodes of boundary-layer flows over a flat plate or a cone at zero angle of attack. In the LST approach, an assumption of locally parallel flow is employed, which is reasonable for the second mode of hypersonic boundary layers since the wave shape of the second mode varies slowly.¹ For second-mode instability, the most-unstable wave is the two-dimensional (2D) wave,¹ and 2D waves are therefore considered in this study. We adopt Cartesian coordinates (x, y) , where x and y denote the streamwise and wall-normal directions, respectively. The second-mode wave is assumed to take the form

$$q'(x, y, t) = \hat{q}(y) \exp(i\alpha x + i\omega t), \quad (6)$$

where q' denotes a perturbation quantity, \hat{q} is the corresponding shape function, t is the time, ω is the angular frequency, and α is the streamwise wavenumber. We consider spatial instability in which ω is a real number and α is a complex number to be solved. Under the assumption of locally parallel boundary-layer flow and neglecting high-order perturbation terms, the small-disturbance governing equations are reduced to ordinary differential equations^{25,26} in the form

$$\frac{d\Psi}{dy} = M\Psi, \quad \Psi = \left[\hat{u}, \frac{d\hat{u}}{dy}, \hat{v}, \hat{p}, \hat{T}, \frac{d\hat{T}}{dy} \right]^T, \quad (7)$$

where M is a 6×6 matrix, \hat{u} and \hat{v} are disturbance velocity components, \hat{p} is the pressure perturbation, \hat{T} is the temperature

perturbation, and the superscript tr denotes the transpose. The non-zero elements of M are given in Appendix A. The mean velocity and temperature profiles utilized in LST are presented in Appendix B. The wall boundary conditions are given by

$$\begin{aligned} y = 0, \quad \hat{u} = \hat{T} = 0, \quad \hat{v} = -\frac{\hat{p}}{Z}, \\ y \rightarrow \infty, \quad \hat{u} = \hat{v} = \hat{T} = 0, \end{aligned} \quad (8)$$

where Z is the specific acoustic impedance. We define the growth rate of perturbations as

$$\sigma = \frac{1}{A} \frac{dA}{dx}, \quad (9)$$

where A is the perturbation amplitude. Then we have $\sigma = -\text{Im}(\alpha)$.

Notably, in the LST calculations, the impedance Z in Eq. (8) is normalized by the free-stream quantities, namely, $\rho_\infty U_\infty$, where U is the streamwise velocity and the subscript ∞ denotes the free stream, rather than by the characteristic specific acoustic impedance of static air, ρc . To straightforwardly correlate with the acoustic characteristics of the metasurface, the impedance Z is normalized by the characteristic specific acoustic impedance at the wall surface, $\rho_w c_w$, and has the form $Z = |Z| \exp(i\varphi)$, where $|Z|$ and φ are the impedance magnitude and phase, respectively. The scale conversion of the characteristic impedance is $\rho_\infty U_\infty / (\rho_w c_w) = M_\infty \sqrt{T_w / T_\infty}$.

C. Direct numerical simulations

We also perform direct numerical simulations (DNS) to evaluate the stabilization performance of the actual metasurface structure. A zero-net-mass-flux actuator²⁷ is placed near the leading edge of the flat plate to generate the disturbances, and the metasurface is mounted flush with the plate. The Navier–Stokes equations for a 2D compressible viscous flow are solved by a homemade parallel multiblock code called PHAROS, which has been successfully employed in hypersonic flow simulations.^{28–30} In the numerical computation, a modified Warming splitting approach is applied to the inviscid terms, and a second-order central difference scheme is utilized to calculate the viscous flux. For the time integration, the explicit three-order Runge–Kutta method is adopted. More details of the simulation algorithm are given in Ref. 30.

The grid size in the double-layer structure is identical to the near-wall grid size of the boundary-layer flow domain, which is fine enough to capture the disturbances transmitted from the boundary-layer flow. However, such a grid also results in an extensive consumption of computational resources. In this study, the metasurface is located in a finite zone where the second-mode waves grow manifestly to save computational resources. The computational configuration and the grid-independent validation of this study are provided in Appendix C.

III. METASURFACE DESIGN

We first evaluate the growth rate of the second mode based on LST and determine the target surface impedance for the metasurface design. We adopt the flow conditions from the experiments by Bountin *et al.*,⁵ namely, free-stream Mach number $M_\infty = 6$, unit Reynolds number $Re_1 = 10.5 \times 10^6 \text{ m}^{-1}$, and temperature $T_\infty = 43.18 \text{ K}$. The wall temperature is constant, $T_w = 293 \text{ K}$. The frequency of the most-unstable second-mode instability experimentally measured by pressure sensors in Ref. 5 is 138.74 kHz. We utilize LST to investigate the effect of

the wall impedance on the growth rate of the second mode within a relatively wide frequency band centered at 138.74 kHz. In addition, the scale conversion of the wall impedance is $\rho_\infty U_\infty / (\rho_w c_w) = M_\infty \sqrt{T_w/T_\infty} = 15.63$.

According to our previous work,¹⁸ an impedance phase $\varphi \in [-45^\circ, 90^\circ]$ is suggested in the design of porous coatings. Essentially, for the scenario of $\varphi \in [-45^\circ, 0^\circ]$, the second mode is mostly stabilized at $\varphi = 0^\circ$. Figure 2 illustrates the distribution of the growth rate of second-mode instability under different impedance magnitudes with impedance phase $\varphi \in [0^\circ, 90^\circ]$. The baseline denotes the smooth-wall case. It can be seen in the smooth-wall case that the second mode is dominant in the region $0.075 \text{ m} \leq x \leq 0.17 \text{ m}$ approximately, where $\sigma > 10 \text{ m}^{-1}$.

The calculation results in Figs. 2(a) and 2(b) reveal that with an increase in the impedance phase from 0° to 90° , the peak growth rate

first decreases and then increases as $\varphi > 30^\circ$. For a fairly small impedance magnitude, the peak of the growth rate shifts further downstream, as shown in Fig. 2(c). Figure 2 also shows that near the leading edge of the flat plate, porous coatings with impedance phase $\varphi \in [0^\circ, 90^\circ]$ will destabilize the hypersonic boundary layer, especially at $\varphi = 0^\circ$, which indicates that a low-impedance boundary near the leading edge is not helpful and may trigger early transition.

From the above results and analysis, it can be concluded that boundaries with small impedance magnitude overall exhibit high efficiency in stabilizing the second mode, except in some special cases. In other words, both the real and imaginary parts of the surface impedance should be small in the porous wall design. The imaginary part of the surface impedance can be well controlled to approach zero by tuning the surface structures to resonance. However, as mentioned above, the real part is determined by the thermal-viscous losses residing in

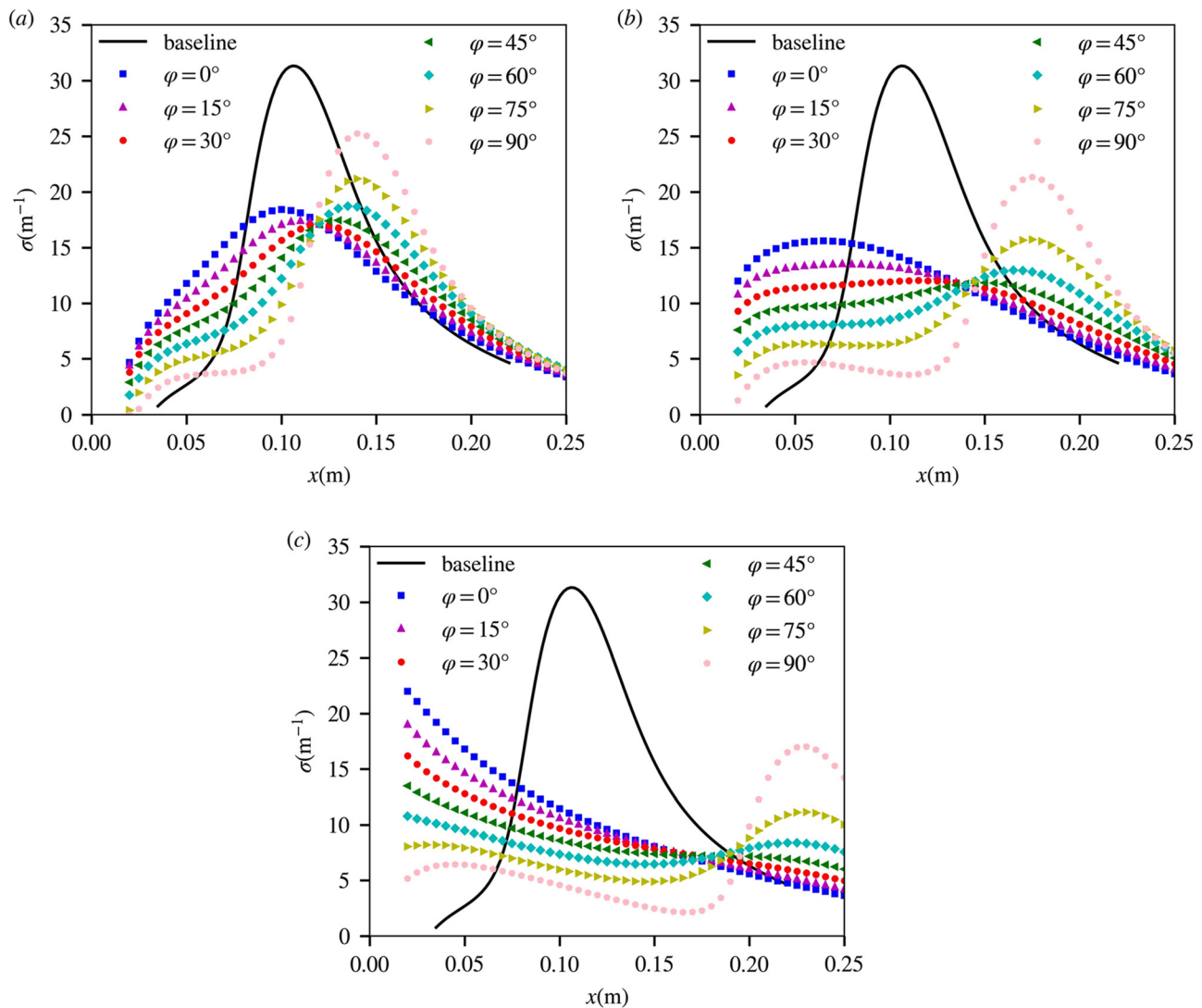


FIG. 2. Distributions of the growth rate of the instability wave at 138.74 kHz for different surface impedance values: (a) $|Z| = 15.63/4$, (b) $|Z| = 15.63/8$, and (c) $|Z| = 15.63/16$. The baseline denotes the smooth-wall case.

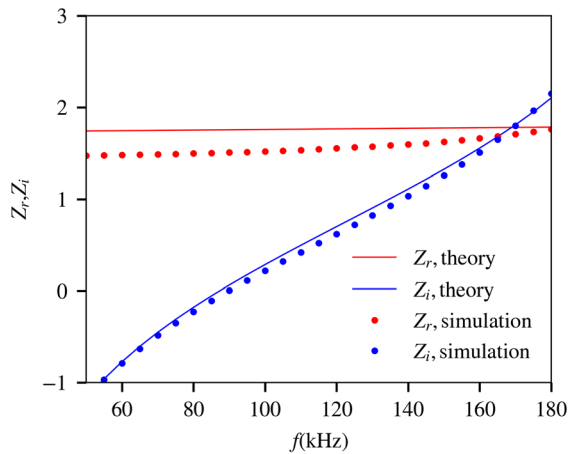


FIG. 3. Broadband resistance and reactance of the acoustic metasurface.

narrow regions, and a relatively large structure is necessary to reduce its value. This will inevitably affect the hypersonic flow field if conventional porous coatings with large grooves or holes are employed. In the following, we demonstrate how the proposed double-layer metasurface can help address this issue.

The growth-rate distribution shown in Fig. 2 indicates that the impedance with magnitude $|Z| = 15.63/8$ and phase φ between 30° and 45° is favorable to second-mode stabilization at $f = 138.74$ kHz and is therefore selected as the target impedance of the metasurface to be designed. We start with the required resistance as given by Eq. (2). In principle, small thickness and large hole diameter lead to a relatively low resistance value. Accordingly, we set $d = 176 \mu\text{m}$, $h = 50 \mu\text{m}$, and nine circular holes ($n = 9$) in a unit cell (cross-sectional area $800 \times 800 \mu\text{m}^2$). Then, the capacitive component of the impedance (negative imaginary part) is proportional to the volume of the back cavity, and so we set the cross-sectional area of the cavity as $S' = 760 \times 760 \mu\text{m}^2$ and its depth as $H = 700 \mu\text{m}$ to adjust the overall acoustic reactance.

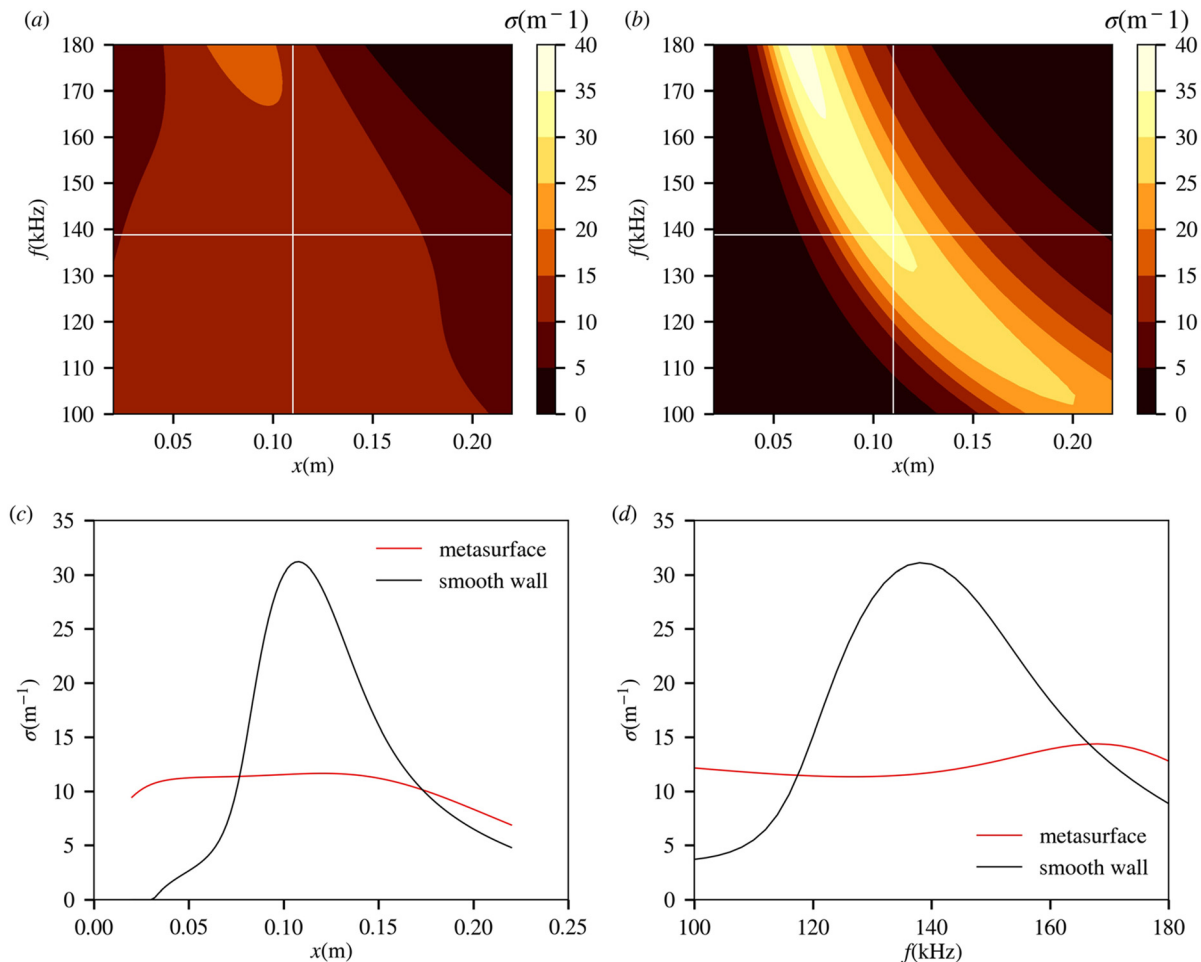


FIG. 4. Comparison of the growth rate of the second mode between the metasurface case and the smooth-wall case using LST. (a) Growth-rate contour plot for the metasurface case. (b) Growth-rate contour plot for the smooth case. (c) Growth rate distribution at $f = 138.74$ kHz (marked by the horizontal lines in the contour plots). (d) Growth rate vs frequency at $x = 0.11$ m (marked by the vertical lines in the contour plots).

The complex impedances obtained from the theoretical model [Eqs. (1)–(5)] and acoustic finite-element simulation in the frequency range of 50–180 kHz are shown in Fig. 3. Overall, the theoretical result is consistent with the simulation result. The discrepancies are due to a simplified coupling effect among the perforations (end correction) in the theoretical model. Clearly, the impedance value at $f = 138.74$ kHz can be easily tuned to meet the above target with relatively small perforations that will not affect the hypersonic flow. As a comparison, Fedorov *et al.*⁹ used porous coatings composed of blind holes with diameter about 50 μm , depth 450 μm , and porosity 0.2 to stabilize the second mode. The resistance reaches as high as 4 with the current wall conditions at $f = 138.74$ kHz. In another work,¹⁶ the resistance value could be reduced to about 1 with the same wall conditions and frequency, but the width, depth, and porosity of the structure became 392 μm , 1.6 mm, and 0.76, respectively. This is already risky in terms of the flow field, since the numerical simulations conducted by Sandham and Lüdtke³¹ showed that the flow becomes noisier when the pore size is as large as one-quarter of the boundary-layer thickness.

It is worth mentioning that the impedance magnitude and phase obtained from the simulation are in the ranges [15.63/10.2, 15.63/5.6] and $[7.2^\circ, 50.4^\circ]$, respectively, for the frequency range of 100–180 kHz, which means that the acoustic metasurface is able to work in a relatively broad band in terms of second-mode control according to Fig. 2. With regard to a possible frequency shift of the most-unstable second mode due to the introduction of the metasurface, Tian *et al.*¹⁸ and Zhu *et al.*³² showed that such a frequency shift emerges when the admittance (or impedance) has an imaginary part that is much larger than its real part, which is not the case for our proposed acoustic metasurface. Practically, the first mode is also important in the hypersonic boundary-layer transition, which is clearly shown in the experimental results of Li *et al.*,³³ where it was found that a glow discharge with a frequency of 12–31 kHz could give rise to a second-mode wave. Fedorov *et al.*⁴ found that a felt-metal coating could stabilize the second mode but excite the first mode. Regarding the proposed acoustic metasurface, the impedance phase indeed

departs greatly from $\varphi = 0^\circ$ for a frequency below 50 kHz, which coincidentally is favorable to stabilization of the first mode.^{11,18}

IV. BROADBAND PERFORMANCE

We now again conduct LST-based calculations, but this time considering the frequency-dependent impedance obtained above rather than a constant impedance value. In these calculations, the surface impedance used in Eq. (8) is obtained from interpolation of the acoustic simulation results given in Fig. 3. As shown in Figs. 4(a) and 4(b), the peak growth rate is significantly diminished in the frequency band of 100–180 kHz compared with the smooth-wall case, indicating that the metasurface can stabilize the Mack second mode in a wide frequency band. Figures 4(c) and 4(b) demonstrate in detail the decrease in the growth rate of the Mack second mode due to the metasurface in the spatial and frequency domains, respectively. It can be seen that the peak growth rate is decreased to nearly one-third of the smooth-wall case by the metasurface in both domains, which represents a similar performance to that reported in Ref. 16.

To further examine the performance of the actual metasurface structure, 2D DNS were conducted with the metasurface consisting of 56 unit cells, located within the region of 0.08–0.125 m. The circular holes of the upper layer were substituted by slits of width 102 μm to maintain the same impedance, with the other sizes of the 2D structure being identical to those of a vertical cut of the 3D structure. Note that the simplification from 3D to 2D here does not change the underlying physics, as has been discussed by Wartemann *et al.*³⁴ Figure 5(a) compares the pressure fluctuations between the smooth wall and metasurface cases at $f = 140$ kHz. It can be seen that the pressure perturbation maintains its growth to the fore and aft of the metasurface region, while in the metasurface region, the pressure fluctuations are clearly attenuated, and the fluctuation intensity grows slowly along the wave propagation direction after a rapid drop. Figure 5(b) presents the broadband performance of the metasurface in stabilizing the Mack second mode. These results confirm that the second-mode perturbations in the

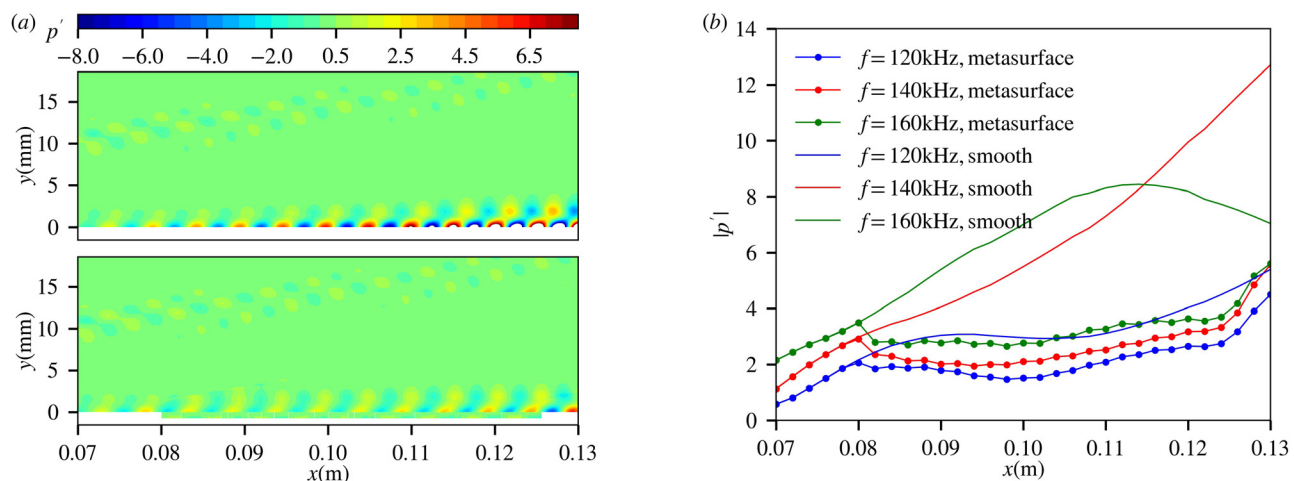


FIG. 5. DNS of the stabilizing effect of the acoustic metasurface. (a) Pressure fluctuation fields for the smooth wall case (top) and the metasurface case (bottom) at $f = 140$ kHz. (b) Pressure fluctuation amplitudes above the smooth wall (solid lines) and the metasurface (lines with symbols) at $f = 120$ kHz (blue lines), 140 kHz (red lines), and 160 kHz (green lines). The pressure fluctuation amplitudes are extracted at $y = 0.1\delta$, where δ is the boundary-layer thickness.

frequency band of 120–160 kHz are substantially suppressed by the metasurface, which clearly validates our design.

V. CONCLUSIONS

In summary, we have designed an acoustic metasurface that is able to stabilize the Mack second mode in hypersonic boundary-layer flow in a relatively wide frequency band. The acoustic metasurface is composed of a perforated layer with micro-holes and a layer with relatively large square cavities. The upper layer has small resistive and inductive components, while the lower cavities work as a capacitive reactance to tune the overall impedance phase. This structure can easily meet the required impedance phase with a minimal effect on the background hypersonic flow field. The proposed acoustic metasurface can be practically implemented by stacking two micro-perforated plates (which are easily fabricated) and attaching them to a rigid wall surface. This work could offer new possibilities for the design of porous coatings for the stabilization of hypersonic boundary layers.

ACKNOWLEDGMENTS

This work was supported by the Research Grants Council of the Hong Kong Special Administrative Region, China (Grant Nos. PolyU 152119/18E and PolyU 15216621) and the National Natural Science Foundation of China (Grant Nos. 51905547, 52078199, and 11872116). T.L. acknowledges support from the National Natural Science Foundation of China (Grant No. 12104383). X.T. acknowledges support from the International Postdoctoral Exchange Fellowship Program (Talent-Introduction Program, Grant No. YJ20210202). This work was carried out in part using computing resources at the High Performance Computing Center of Central South University.

AUTHOR DECLARATIONS

Conflict of Interest

The authors have no conflicts to disclose.

Author Contributions

Xudong Tian: Conceptualization (supporting); Data curation (lead); Formal analysis (lead); Funding acquisition (supporting); Investigation (lead); Methodology (lead); Resources (equal); Software (lead); Validation (lead); Visualization (lead); Writing – original draft (lead); Writing – review and editing (lead). **Tuo Liu:** Conceptualization (lead); Formal analysis (lead); Funding acquisition (supporting); Investigation (equal); Methodology (equal); Project administration (lead); Resources (supporting); Software (equal); Supervision (equal); Validation (equal); Visualization (supporting); Writing – original draft (lead); Writing – review and editing (lead). **Tiantian Wang:** Formal analysis (supporting); Funding acquisition (supporting); Project administration (supporting); Resources (equal); Supervision (supporting); Writing – original draft (supporting); Writing – review and editing (supporting). **Jie Zhu:** Conceptualization (supporting); Formal analysis (supporting); Funding acquisition (lead); Project administration (equal); Resources (supporting); Supervision (lead); Writing – original draft (supporting); Writing – review and editing (supporting). **Chihyung Wen:** Formal analysis (supporting); Funding acquisition (supporting); Project administration (supporting); Resources

(supporting); Supervision (supporting); Writing – original draft (supporting); Writing – review and editing (supporting).

DATA AVAILABILITY

The data that support the findings of this study are available from the corresponding authors upon reasonable request.

APPENDIX A: ELEMENTS OF MATRIX M

The nonzero elements of the matrix M in Eq. (7) are

$$\begin{aligned}
 M_{12} &= M_{56} = 1, \\
 M_{21} &= \alpha^2 + \frac{i(\alpha U + \omega)R}{\mu T}, \\
 M_{22} &= -\frac{1}{\mu} \frac{d\mu}{dy}, \quad M_{23} = -i\alpha \left(\frac{1}{3T} \frac{dT}{dy} + \frac{1}{\mu} \frac{d\mu}{dy} \right) + \frac{R}{\mu T} \frac{dU}{dy}, \\
 M_{24} &= \frac{i\alpha R}{\mu} - \frac{\gamma M_e^2 \alpha (\alpha U + \omega)}{3}, \\
 M_{25} &= \frac{\alpha (\alpha U + \omega)}{3T} - \frac{1}{\mu} \frac{d}{dy} \left(\frac{d\mu}{dT} \frac{dU}{dy} \right), \quad M_{26} = -\frac{1}{\mu} \frac{d\mu}{dy} \frac{dU}{dy}, \\
 M_{31} &= -i\alpha, \quad M_{33} = \frac{1}{T} \frac{dT}{dy}, \quad M_{34} = -i\gamma M_e^2 (\alpha U + \omega), \\
 M_{35} &= \frac{i(\alpha U + \omega)}{T}, \\
 M_{41} &= -i\chi \alpha \left(\frac{4}{3T} \frac{dT}{dy} + \frac{2}{\mu} \frac{d\mu}{dy} \right), \\
 M_{42} &= -i\alpha \chi, \\
 M_{43} &= -\frac{4}{3} i\chi \gamma M_e^2 \left[\alpha \frac{dU}{dy} + (\alpha U + \omega) \left(\frac{1}{T} \frac{dT}{dy} + \frac{1}{\mu} \frac{d\mu}{dy} \right) \right], \\
 M_{45} &= i\chi \left[\alpha \left(\frac{4}{3T} + \frac{1}{\mu} \frac{d\mu}{dT} \right) \frac{dU}{dy} + \frac{4(\alpha U + \omega)}{3\mu T} \frac{d\mu}{dy} \right], \\
 M_{46} &= \frac{4i\chi (\alpha U + \omega)}{3T}, \\
 M_{62} &= -2Pr(\gamma - 1) M_e^2 \frac{dU}{dy}, \\
 M_{63} &= \frac{RPr}{\mu T} \frac{dT}{dy} - 2i\alpha(\gamma - 1) M_e^2 Pr \frac{dU}{dy}, \\
 M_{64} &= -\frac{iRPr(\gamma - 1) M_e^2 (\alpha U + \omega)}{\mu}, \\
 M_{65} &= \alpha^2 + \frac{iRPr(\alpha U + \omega)}{\mu T} - \frac{(\gamma - 1) M_e^2 Pr}{\mu} \frac{d\mu}{dT} \left(\frac{dU}{dy} \right)^2 - \frac{1}{\mu} \frac{d^2\mu}{dy^2}, \\
 M_{66} &= -\frac{2}{\mu} \frac{d\mu}{dy},
 \end{aligned}$$

where $\chi = [R/\mu + 4i\gamma M_e^2(\alpha U + \omega)/3]^{-1}$; U and T are the mean velocity and temperature, respectively; μ is the dynamic viscosity (which is temperature-dependent); γ , R , and Pr are the specific heat ratio, Reynolds number, and Prandtl number, respectively; and M_e is the Mach number at the boundary-layer edge. Here Stokes's hypothesis has been employed.

APPENDIX B: MEAN VELOCITY AND TEMPERATURE PROFILES

The mean velocity and temperature profiles employed in the LST are shown in Fig. 6.

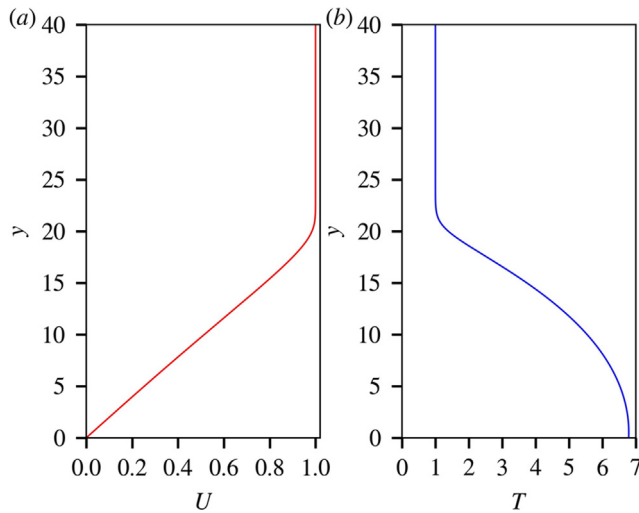


FIG. 6. (a) Mean velocity and (b) mean temperature profiles employed in the LST. The profiles are normalized by the values at the boundary-layer edge, U_e and T_e , respectively; the distance y from the wall is normalized by the boundary-layer thickness length scale $\sqrt{x\mu/(\rho U_e)}$.

APPENDIX C: COMPUTATIONAL CONFIGURATION AND NUMERICAL VALIDATION

In this study, a hypersonic boundary layer over a flat plate is numerically simulated. Figure 7 illustrates the computational configuration. The disturbance actuator located near the leading edge is described by

$$(\rho v)_w = \varepsilon(\rho U)_\infty \sin\left(2\pi \frac{x - x_1}{x_2 - x_1}\right) \sin(2\pi ft), \quad (\text{C1})$$

where $\varepsilon = 0.001$, $x_1 = 0.01$ m, and $x_2 = 0.015$ m. The metasurface is located from $x = 0.08$ m to $x = 0.125$ m.

DNS of second-mode propagation along a smooth flat plate was discussed in detail in Ref. 30. Here we perform a grid-independence verification to confirm the effectiveness of our simulations. Two mesh sizes, a medium mesh (about 1.57×10^6 mesh elements) and a refined mesh (about 2.5×10^6 mesh elements), are considered in our verification. As shown in Fig. 8, the two mesh

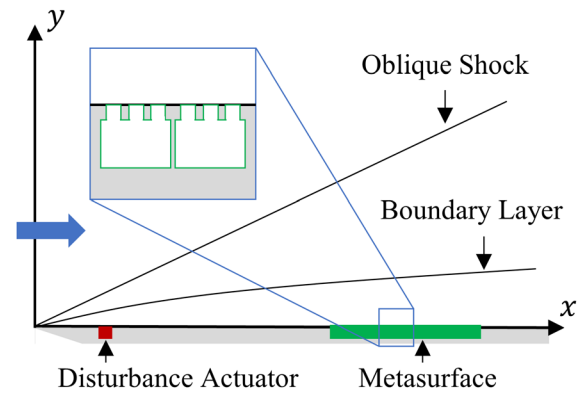


FIG. 7. Schematic of the computational configuration. The flat plate has length 0.28 m, and the metasurface is located from $x = 0.08$ m to $x = 0.125$ m. The upper layer contains three slits of width $102 \mu\text{m}$ in each unit cell.

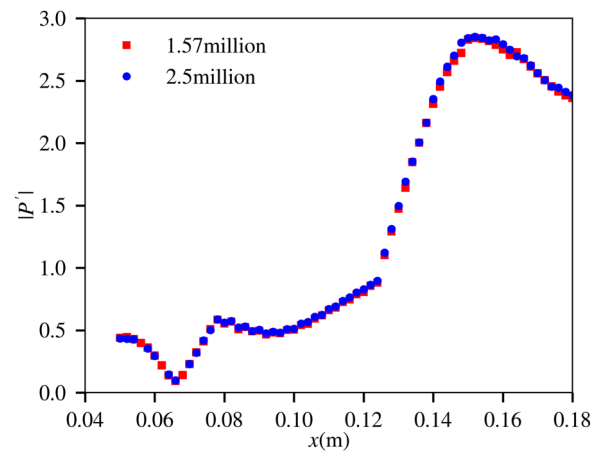


FIG. 8. Comparison of the fluctuating pressure amplitudes obtained from the medium and refined meshes.

sizes produce consistent results. The medium mesh is therefore employed in this study to save computational resources.

REFERENCES

- ¹L. M. Mack, *Boundary-Layer Linear Stability Theory* (California Institute of Technology, Pasadena Jet Propulsion Lab, 1984).
- ²K. Stetson, E. Thompson, J. Donaldson, and L. Siler, "Laminar boundary layer stability experiments on a cone at Mach 8. Part I: Sharp cone," AIAA Paper No. 83-1761, 1983.
- ³K. Stetson and R. Kimmel, "On hypersonic boundary-layer stability," AIAA Paper No. 92-0737, 1992.
- ⁴A. V. Fedorov, A. Shiplyuk, A. Maslov, E. Burov, and N. Malmuth, "Stabilization of a hypersonic boundary layer using an ultrasonically absorptive coating," *J. Fluid Mech.* **479**, 99 (2003).
- ⁵D. Bountin, T. Chimitov, A. Maslov, A. Novikov, I. Egorov, A. Fedorov, and S. Utyuzhnikov, "Stabilization of a hypersonic boundary layer using a wavy surface," *AIAA J.* **51**, 1203 (2013).
- ⁶S. J. Laurence, A. Wagner, and K. Hannemann, "Experimental study of second-mode instability growth and breakdown in a hypersonic boundary layer using high-speed schlieren visualization," *J. Fluid Mech.* **797**, 471 (2016).

- ⁷A. V. Fedorov, N. D. Malmuth, A. Rasheed, and H. G. Hornung, "Stabilization of hypersonic boundary layers by porous coatings," *AIAA J.* **39**, 605 (2001).
- ⁸A. Rasheed, H. G. Hornung, A. V. Fedorov, and N. D. Malmuth, "Experiments on passive hypervelocity boundary-layer control using an ultrasonically absorptive surface," *AIAA J.* **40**, 481 (2002).
- ⁹A. Fedorov, V. Kozlov, A. Shiplyuk, A. Maslov, and N. Malmuth, "Stability of hypersonic boundary layer on porous wall with regular microstructure," *AIAA J.* **44**, 1866 (2006).
- ¹⁰A. Wagner, M. Kuhn, J. Martinez Schramm, and K. Hannemann, "Experiments on passive hypersonic boundary layer control using ultrasonically absorptive carbon-carbon material with random microstructure," *Exp. Fluids* **54**, 1606 (2013).
- ¹¹X. Tian and C. Wen, "Growth mechanisms of second-mode instability in hypersonic boundary layers," *J. Fluid Mech.* **908**, R4 (2021).
- ¹²R. Zhao, C. Wen, Y. Zhou, G. Tu, and J. Lei, "Review of acoustic metasurfaces for hypersonic boundary layer stabilization," *Prog. Aerosp. Sci.* **130**, 100808 (2022).
- ¹³G. A. Brès, T. Colonius, and A. V. Fedorov, "Acoustic properties of porous coatings for hypersonic boundary-layer control," *AIAA J.* **48**, 267 (2010).
- ¹⁴G. A. Brès, M. Inkman, T. Colonius, and A. V. Fedorov, "Second-mode attenuation and cancellation by porous coatings in a high-speed boundary layer," *J. Fluid Mech.* **726**, 312 (2013).
- ¹⁵R. Zhao, T. Liu, C. Y. Wen, J. Zhu, and L. Cheng, "Theoretical modeling and optimization of porous coating for hypersonic laminar flow control," *AIAA J.* **56**, 2942 (2018).
- ¹⁶R. Zhao, T. Liu, C. Wen, J. Zhu, and L. Cheng, "Impedance-near-zero acoustic metasurface for hypersonic boundary-layer flow stabilization," *Phys. Rev. Appl.* **11**, 044015 (2019).
- ¹⁷B. Assouar, B. Liang, Y. Wu, Y. Li, J.-C. Cheng, and Y. Jing, "Acoustic metasurfaces," *Nat. Rev. Mater.* **3**, 460 (2018).
- ¹⁸X. Tian, R. Zhao, T. Long, and C. Y. Wen, "Reverse design of ultrasonic absorptive coating for the stabilization of Mack modes," *AIAA J.* **57**, 2264 (2019).
- ¹⁹K. Fujii, "Experiment of the two-dimensional roughness effect on hypersonic boundary-layer transition," *J. Spacecr. Rockets* **43**, 731 (2006).
- ²⁰D. Y. Maa, "Potential of microperforated panel absorber," *J. Acoust. Soc. Am.* **104**, 2861 (1998).
- ²¹Y. Li and B. M. Assouar, "Acoustic metasurface-based perfect absorber with deep subwavelength thickness," *Appl. Phys. Lett.* **108**, 063502 (2016).
- ²²J. S. Bolton and N. Kim, "Use of CFD to calculate the dynamic resistive end correction for microperforated materials," *Acoust. Aust.* **38**(3), 134–139 (2010).
- ²³V. Naderyan, R. Raspet, C. J. Hickey, and M. Mohammadi, "Acoustic end corrections for micro-perforated plates," *J. Acoust. Soc. Am.* **146**, EL399 (2019).
- ²⁴B. H. Song and J. S. Bolton, "A transfer-matrix approach for estimating the characteristic impedance and wave numbers of limp and rigid porous materials," *J. Acoust. Soc. Am.* **107**, 1131 (2000).
- ²⁵M. R. Malik, "Numerical methods for hypersonic boundary layer stability," *J. Comput. Phys.* **86**, 376 (1990).
- ²⁶A. Tumin, "Three-dimensional spatial normal modes in compressible boundary layers," *J. Fluid Mech.* **586**, 295 (2007).
- ²⁷R. Zhao, C. Y. Wen, X. D. Tian, T. H. Long, and W. Yuan, "Numerical simulation of local wall heating and cooling effect on the stability of a hypersonic boundary layer," *Int. J. Heat Mass Transfer* **121**, 986 (2018).
- ²⁸J. Hao, J. Wang, and C. Lee, "Numerical simulation of high-enthalpy hollow-cylinder/flare flows," *AIAA J.* **56**, 3337 (2018).
- ²⁹J. Hao, J. Wang, and C. Lee, "Numerical simulation of high-enthalpy double-cone flows," *AIAA J.* **55**, 2471 (2017).
- ³⁰J. Hao and C.-Y. Wen, "Stabilization of a two-dimensional hypersonic boundary layer using a shallow cavity," *AIAA J.* **59**, 430 (2021).
- ³¹N. D. Sandham and H. Lüdeke, "Numerical study of Mach 6 boundary-layer stabilization by means of a porous surface," *AIAA J.* **47**, 2243 (2009).
- ³²W. Zhu, X. Chen, Y. Zhu, and C. Lee, "Nonlinear interactions in the hypersonic boundary layer on the permeable wall," *Phys. Fluids* **32**(10), 104110 (2020).
- ³³C. Li, Y. Zhang, and C. Lee, "Influence of glow discharge on evolution of disturbance in a hypersonic boundary layer: The effect of first mode," *Phys. Fluids* **32**(5), 051701 (2020).
- ³⁴V. Wartemann, H. Lüdeke, and N. D. Sandham, "Numerical investigation of hypersonic boundary-layer stabilization by porous surfaces," *AIAA J.* **50**, 1281 (2012).